Structurally Designed Synthesis of Mechanically Stable Poly(benzoxazine-co-resol)-Based Porous Carbon Monoliths and Their Application as High-Performance CO2 Capture Sorbents

10 AUTHORS, INCLUDING:

Guang-Ping Hao
Technische Universität Dresden
32 PUBLICATIONS **1,108** CITATIONS

SEE PROFILE

Tao Zhang
Fudan University
890 PUBLICATIONS **17,319** CITATIONS

SEE PROFILE

H J Bongard
Max Planck Institute for Coal Research
44 PUBLICATIONS **1,098** CITATIONS

SEE PROFILE

An-Hui Lu
Dalian University of Technology
133 PUBLICATIONS **8,114** CITATIONS

SEE PROFILE

Structurally Designed Synthesis of Mechanically Stable Poly(benzoxazine-co-resol)-Based Porous Carbon Monoliths and Their Application as High-Performance CO2 Capture Sorbents

Guang-Ping Hao,[†] Wen-Cui Li,[†] Dan Qian,[†] Guang-Hui Wang,[†] Wei-Ping Zhang,[‡] Tao Zhang,[‡] Ai-Qin Wang,[‡] Ferdi Schüth,[§] Hans-Josef Bongard,[§] and An-Hui Lu*,[†]

[†]State Key Laboratory of Fine Chemicals, School of Chemical Engineering, Dalian University of Technology, Dalian 116024, P. R. China

[‡]State Key Laboratory of Catalysis, Dalian Institute of Chemical Physics, Chinese Academy of Sciences, Dalian 116023, P. R. China

[§]Max-Planck-Institut für Kohlenforschung, D-45470 Mülheim an der Ruhr, Germany

S *Supporting Information*

ABSTRACT: Porous carbon monoliths with defined multi-length scale pore structures, a nitrogen-containing framework, and high mechanical strength were synthesized through a self-assembly of poly(benzoxazine-co-resol) and a carbonization process. Importantly, this synthesis can be easily scaled up to prepare carbon monoliths with identical pore structures. By controlling the reaction conditions, porous carbon monoliths exhibit fully interconnected macroporosity and mesoporosity with cubic *Im3m* symmetry and can withstand a press pressure of up to 15.6 MPa. The use of amines in the synthesis results in a nitrogen-containing framework of the carbon monolith, as evidenced by the cross-polarization magic-angle-spinning NMR characterization. With such designed structures, the carbon monoliths show outstanding CO_2 capture and separation capacities, high selectivity, and facile regeneration at room temperature. At ~1 bar, the equilibrium capacities of the monoliths are in the range of 3.3−4.9 mmol g^{-1} at 0 °C and of 2.6−3.3 mmol g^{-1} at 25 °C, while the dynamic capacities are in the range of 2.7−4.1 wt % at 25 °C using 14% (v/v) CO_2 in N_2. The carbon monoliths exhibit high selectivity for the capture of CO_2 over N_2 from a CO_2/N_2 mixture, with a separation factor ranging from 13 to 28. Meanwhile, they undergo a facile CO_2 release in an argon stream at 25 °C, indicating a good regeneration capacity.
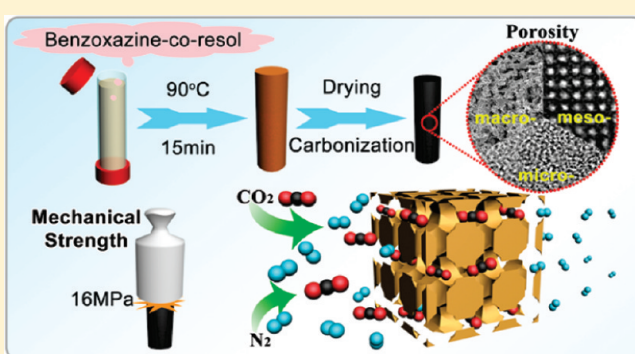
1. INTRODUCTION

The selective capture and separation of carbon dioxide (CO_2) in an economical and energy-efficient fashion have attracted tremendous attention, due to the dual roles of CO_2 as a greenhouse gas and a renewable carbon source.[1−3] In particular, selective capture of CO_2 from power plant flue gas (comprising ~70% N_2 and ~15% CO_2, pressure of ~1 bar) emissions is a hot issue and still remains challenging.[4,5] In recent years, a number of CO_2 capture porous solids have been developed,[6−8] including porous carbons,[9−16] zeolites (e.g., 13X, 5A, natrolite),[17−19] amine-modified silicas,[20−25] and new classes of hybrid crystalline solids (e.g., MOFs, ZIFs, COFs, MCPs, PCPs).[5,26−35] Among them, porous carbons with high surface area, good chemical resistance to both alkaline and acidic media, and excellent thermal stability are most suitable for CO_2 capture used in a wide range of operating conditions.[36−38]

Commercial activated carbons (including Norit R1 Extra, BPL, Maxsorb, A10 fiber and activated carbon A) commonly possess a high surface area (1000−3100 m^2 g^{-1}) with an abundant microporosity (0.4−1.4 cm^{3}g^{-1}). They exhibit a larger adsorption capacity for CO_2 at high pressures but lower at low relative pressures.[10,11] In order to improve their CO_2 sorption performance, especially at low pressures, amine groups have been introduced into the porous carbons, by either postmodification or copolymerization of amine-containing precursors.[12,14−16] For example, the monoethanolamine impregnated activated carbons show enhanced CO_2 capacity (75 mg g^{-1}) at 75 °C and 1 bar as compared to the parent support (31 mg g^{-1}).[14] Similarly, the amino-rich carbon obtained by a postmodification of glucose carbon with a branched tetramine, gives a high sorption capability for CO_2 (4.3 mmol g^{-1} at −20 °C and 1 bar) despite possessing a very low surface area (<20 m^2 g^{-1}).[15] Alternatively, the nitrogen-enriched carbon can be prepared by carbonization of melamine and formaldehyde resin polymerized using fumed silica as porogen through a nanocasting pathway, and it also shows a high CO_2 capture capacity of 2.25 mmol g^{-1} at 25 °C.[16] Obviously, chemisorption of CO_2 through grafted oligoamine

Table 1. Synthesis Conditions and Textural Parameters of the Porous Carbon Monoliths[a]

Sample	amines	Molar ratio of R/amine/F127	S_{BET} (m² g⁻¹)	D_{meso} (nm)	V_{total} (cm³ g⁻¹)	V_{mic} (cm³ g⁻¹)	P[b] (MPa)
HCM-DAH-1	DAH	275:6.8:1	670	5.0	0.46	0.20	15.6
HCM-EDA	EDA	275:5.3:1	639	4.8	0.35	0.24	0.3
HCM-DMA	DMA	275:6.5:1	607	3.5	0.22	0.11	0.2
HCM-TMA	TMA	275:12.5:1	623	—	0.32	0.26	0.6
HCM-TEA	TEA	275:5.0:1	586	—	0.25	0.10	0.7
HCM-DAH-0.38	DAH	275:2.6:1	609	4.9	0.41	0.18	15.7
HCM-DAH-2	DAH	275:13.6:1	596	5.4	0.36	0.20	14.7
HCM-DAH-4	DAH	275:27.2:1	540	4.9	0.30	0.20	4.8
HCM-DAH-8	DAH	275:54.4:1	505	12.0	0.30	0.20	0.8
HCM-DAH-16	DAH	275:171.4:1					

[a] The pH of the reaction solution of HCM-EDA, HCM-DMA, HCM-TMA, and HCM-TEA, before adding CH_2O, is almost identical to that of HCM-DAH-1. [b] The applied pressure when a carbon monolith starts to crack, which reflects the mechanical stability of the carbon monolith.

moieties on the carbon is thus a straightforward approach. However, the regeneration of these amine-modified sorbents requires a large amount of pressure and/or a high temperature gradient to enable a complete desorption of CO_2. Moreover, most carbonaceous CO_2 sorbents are predominantly in powder form and thus accompanied with some potential physicochemical drawbacks such as high-pressure drop, low heat and mass transfer, and mechanical attrition.[39−42] In addition, most of the studies have been limited to equilibrium uptake measurements, rather than the more industrially relevant dynamic capacity and regeneration. Hence, it is more attractive to develop an efficient synthesis for monolithic porous carbons with a controllable structure and good mechanical strength. Such carbon monoliths should exhibit high reversible capacity and selectivity as well as good regeneration ability at ambient temperature and pressure and overcome the problems caused by powder carbons.

A CO_2 molecule has a large electric quadrupole moment that arises from the strong dipole moments of the C=O bonds. Considering the polarizabilities and the kinetic diameters of CO_2 (29.11×10^{-25} cm³, 3.3 Å) and N_2 (17.40×10^{-25} cm³, 3.6−3.8 Å),[43,44] high-performance sorbents for CO_2 capture and separation from flue gases should possess the intrinsic properties such as an abundance of micropores and a polar surface. From the diffusion kinetics point of view, a highly interconnected, hierarchical pore system is highly required for rapid gas transport. Keeping this in mind, we designed a targeted synthesis of poly-(benzoxazine-co-resol)-based porous carbon monoliths with multiple-length-scale porosity (macro-, meso-, and micropores), a nitrogen-containing framework (polar surface), and remarkable mechanical strength. The newly developed poly(benzoxazine-co-resol) offers a high degree of flexibility in the molecular design of monomers, which are based on phenols, aldehydes, and diamines (nitrogen source).[45−47] The obtained carbon monoliths show excellent performance in CO_2 capture and separation. Both equilibrium and dynamic capacities and selectivity are highest by far among the reported CO_2 capture carbon materials and they can be facilely regenerated.

2. EXPERIMENTAL SECTION

2.1. Chemicals. Resorcinol (denoted R, 99.5%) and formalin (37 wt %) were purchased from Tianjin Kermel Chemical Reagent Co., Ltd. 1,6-Diaminohexane (DAH, 99.0%), ethylenediamine (EDA, 99.0%), dimethylamine (DMA, 33%), trimethylamine (TMA, 33%),

triethylamine (TEA, 99.0%), and ethanol (99.7%) were supplied by Sinopharm Chemical Reagent Co., Ltd. Pluronic F127 was purchased from Fluka. All chemicals were used as received.

2.2. Synthesis of Monolithic Carbons. Typically, 3.0 g of resorcinol (27.3 mmol) and 1.25 g of Pluronic F127 were dissolved in an 18 g solvent mixture of ethanol (11.4 mL) and deionized water (9 mL) with magnetic stirring at 25 °C. Afterward, 0.078 g of 1, 6-diaminohexane (0.67 mmol) was added to the above solution and stirred for *ca.* 30 min at 25 °C until the solution turned pale yellow. Subsequently, 4.42 g of formalin (37 wt %) containing formaldehyde (denoted F, 1.64 g, 54.5 mmol) was quickly injected into the solution. The reaction system instantaneously (<1 min) turned to a white homogeneous emulsion, and the reaction mixture was stirred at 25 °C for another 10 min. The white homogeneous emulsion was then sealed and transferred into an oven at 90 °C. It quickly turned yellow and solidified within 15 min. This gel was cured for an additional 4 h.

The as-made polymer monolith (denote HPM) was first dried at 50 °C for 24 h, followed by pyrolysis at 800 °C for 2 h under a nitrogen atmosphere to obtain a crack-free porous carbon monolith (denoted HCM-DAH-1). By varying the amount of DAH (see Table 1), different polymer monoliths were prepared. In all syntheses, the molar ratio of R/F127 was fixed as 275:1 and R/F as 1:2. The mass ratio between water and ethanol was fixed at 1:1. The obtained monoliths were denoted HCM-DAH-x, where x indicates the multiples of the amount of the organic amine DAH used for sample HCM-DAH-1.

For comparison, besides DAH, four additional organic amines, including EDA, DMA, TMA, and TEA, were used to prepare porous carbon monoliths. The synthesis procedure is essentially the same as that described above. Particular attention was paid to adjust the pH of the reaction solution to the same value as that in the synthesis of HCM-DAH-1 by adjusting the amounts of the organic bases. The obtained carbon monoliths were denoted HCM-y, where y = EDA, DMA, TMA, or TEA.

2.3. Characterization. Low angle X-ray diffraction (XRD) patterns of samples were recorded with a STOE STADI P diffractometer in the Bragg−Brentano (reflection) geometry using Cu K_α radiation. The d-spacing values were calculated from the formula $d = \lambda/2 \sin \theta$, and the unit cell parameters were calculated from the formula $a_0 = 2d_{110}/\sqrt{3}$. Transmission electron microscope (TEM) images of the samples were obtained with a Tecnai G²20S-Twin electron microscope equipped with a cold field emission gun. The acceleration voltage was 200 kV. Samples were prepared on a lacey carbon film supported by a copper grid. Scanning electron microscope (SEM) investigations were carried out with a Hitachi S-4800 instrument, and a Hitachi S-5500 microscope operated at 30 kV.
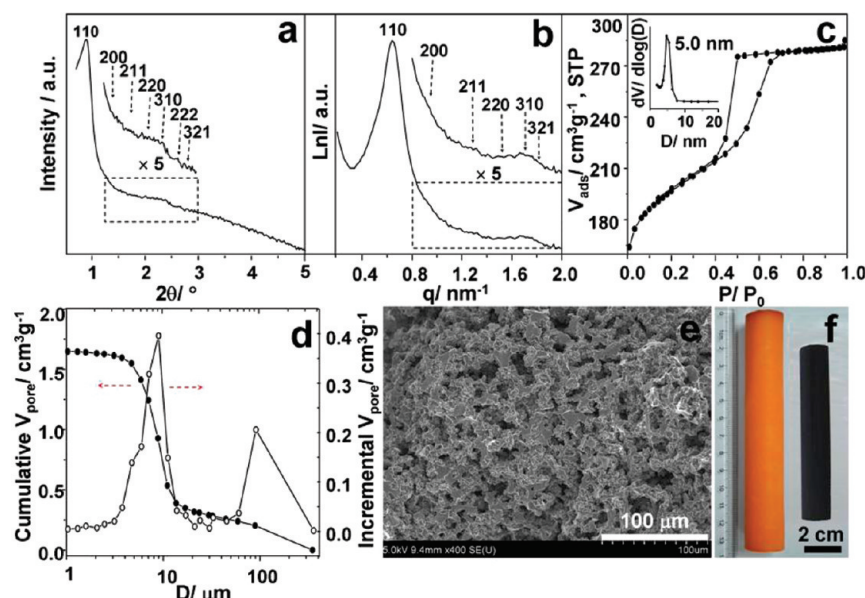
Figure 1. Results of structural characterization of sample HCM-DAH-1: (a) low-angle XRD and (b) SAXS pattern, (c) N_2 isotherm and the corresponding PSD (inset), (d) Hg intrusion curve and differential PSD, (e) SEM image, and (f) representative photograph of the synthesized polymer and carbon monoliths.

Nitrogen adsorption isotherms were measured with an ASAP 2020 sorption analyzer (Micromeritics). The Brunauer–Emmett–Teller (BET) method was utilized to calculate the specific surface areas (S_{BET}). Pore size distributions (PSDs) were determined from the adsorption branches of the isotherms using Density Functional Theory (DFT) and the Barrett–Joyner–Halenda (BJH) model for micropores and mesopores, respectively. Total pore volumes (V_{total}) were calculated from the amount adsorbed at a relative pressure, P/P_0 of 0.97. Micropore volumes (V_{micro}) were calculated using the t-plot method. Hg intrusion isotherms and PSDs of the pores larger than 50 nm were measured using a Micromeritics AutoPore IV 9500 analyzer.

^{1}H→^{13}C cross-polarization magic-angle-spinning (CP/MAS) NMR experiments were performed on a Varian Infinityplus-400 spectrometer equipped with a 5 mm MAS probe. The spectra were recorded at 100.5 MHz with a spinning rate of 11 kHz, 2000–3600 scans, a contact time of 3 ms, and a recycle delay of 4 s. The chemical shifts of ^{13}C NMR spectra were referenced to tetramethylsilane. Before the CP/MAS NMR measurements, the polymer monolith was ground into fine powders. Elemental analysis was carried out on an elemental analyzer (Vario EL III, Elementar). The thermal decomposition behavior of the products was monitored using a simultaneous thermal analyzer (Netzsch STA 449 F3) from 30 to 800 °C under nitrogen with a heating rate of 10 °C/min.

The mechanical properties of the samples were tested under uniaxial compression using a 2 kN intelligent strength tester (model DL III, Dalian Research & Design Institute of Chemical Industry). The compressive strength is the maximum stress supported by the samples during the test, i.e., the stress at which macroscopic failure occurs. Tests were performed at a strain rate of 1 mm/min. All measurements were recorded at ca. 30 °C and 80% relative humidity. Samples were cylinders carefully machined to have perfectly parallel bases and a length/diameter ratio of 1. No precautions were taken to prevent moisture adsorption by the carbon monoliths.

2.4. CO_2 Sorption and Separation Measurements. Equilibrium Gas Adsorption Measurements: The gas adsorption isotherms of the HCM series were measured using a Micromeritics ASAP 2020 static volumetric analyzer at the setting temperature. Prior to each adsorption experiment, the sample was degassed for 6 h at 200 °C ensuring that the residual pressure fell below 5×10^{-3} mbar and then cooled down to the

target temperature, followed by introduction of a single component gas (CO_2 or N_2) into the system. The gas adsorption capacity in terms of adsorbed volume under standard temperature and pressure (STP) was then recorded.

Dynamic Gas Separation Measurements: The separation of CO_2 from the CO_2–N_2 binary mixture was performed in a fixed-bed flow sorber (a stainless steel tube with an inner diameter of 9 mm and a length of 100 mm) operated at ∼1 bar, 25 °C, which was controlled by a pressure controller and a thermostatic water bath, respectively (see Supporting Information for more details). The sorbent bed was first heated to 200 °C in Ar at a flow rate of 100 mL/min and held for 30 min. Breakthrough experiments were carried out by switching abruptly from Ar to a 14% mixture of CO_2 in N_2 and at a flow rate of 7 mL/min. The treated gas out of the sorber was monitored online by using an Agilent 7890A gas chromatograph with a TCD detector.

3. RESULTS AND DISCUSSION

3.1. Structural Properties of the Porous Carbon Monolith. The newly developed poly(benzoxazine-co-resol) offers a remarkable opportunity for the molecular design of a nitrogen-containing polymer. The basic sites of nitrogen-containing groups are beneficial for enhancing CO_2 adsorption. Meanwhile, to minimize molecular diffusion limitation, it is an essential necessity to create highly interconnected macropores and mesopores in porous carbons. Under this consideration, we herein attempted to introduce surfactant Pluronic F127 in the reaction system to direct the formation of interconnected mesopores (cuibic *Im3m* symmetry) during the assembly of poly(benzoxazine-co-resol). The resultant carbon monolith HCM-DAH-1 was characterized with various analytical techniques. As seen in Figure 1a, the low-angle XRD pattern of HCM-DAH-1 shows well-resolved reflections, which can be indexed as (110), (200), (211), (220), (310), (222), and (321) based on a body-centered cubic symmetry (*Im3m*). The intense (110) peak corresponds to a *d*-spacing of 9.6 nm, from which a unit cell parameter of 11.1 nm can be calculated. The small-angle X-ray scattering
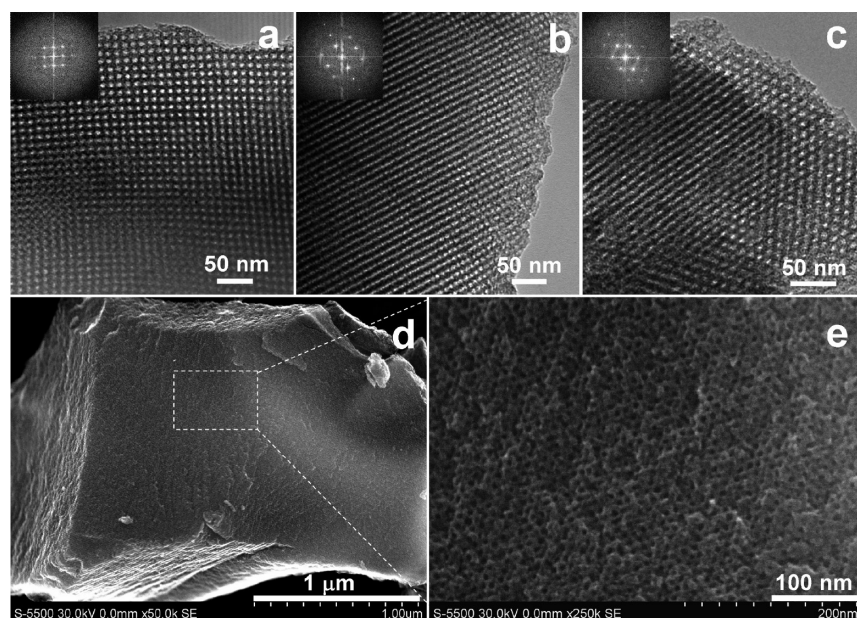
Figure 2. TEM images (a, b, and c: images viewed in the [100], [110], and [111] direction; the insets are the corresponding fast Fourier transform (FFT) diffractograms) and HR-SEM images (d, e) of carbon monolith HCM-DAH-1.

(SAXS) pattern of HCM-DAH-1 (Figure 1b) also shows well-defined reflections, which can be indexed as (110), (200), (211), (220), (310), and (321) and again associated with a body-centered cubic $Im3m$ symmetry.

The porous structure of HCM-DAH-1 was analyzed by N_2 adsorption at 77 K. As shown in Figure 1c, the isotherm of HCM-DAH-1 is of type IV in shape with a type H2 hysteresis loop, which is typical for a mesoporous material with a 3D caged pore structure.[48] The PSDs (Figure 1c, inset) show that the mesopores are concentrated at a size of ~5.0 nm. The specific surface area and pore volume are 670 $m^2\,g^{-1}$ and 0.46 $cm^3\,g^{-1}$, respectively (Table 1).

The presence of macroporosity in HCM-DAH-1 was confirmed by Hg intrusion analysis. As shown in Figure 1d, the curve of cumulative pore volume vs pore diameter shows a continuous increase in mercury uptake with a decrease in pore diameter (i.e., increase of Hg intrusion pressure). When the pores are close to ca. 3.8 μm in diameter, a plateau characterized with a saturation Hg uptake of 1.67 $cm^3\,g^{-1}$ was reached. This indicates that HCM-DAH-1 possesses abundant and fully interconnected macroporosity and a large macropore volume. The macropore sizes are concentrated at ~9.1 μm. The cocontinuous macropores were formed due to the polymerization-induced phase separation. Micrometer-range heterogeneity composed of gel and fluid phases was first generated and then the conjugate fluid phase (solvents) were removed, leaving the cocontinuous macropore spaces.[49,50] Noticeably, our monolith shows a much larger total pore volume and macropore size than those of phenolic-based mesoporous carbons (total pore volume 1.14 $cm^3\,g^{-1}$ and macropore size 3 μm).[51] The SEM image (Figure 1e) confirms that carbon monolith HCM-DAH-1 exhibits fully interconnected macroporosity and a robust sponge-like branched skeleton. This is consistent with the Hg intrusion analysis. The macroscopical photograph (Figure 1f) shows that both the polymer monolith (HPM-1) and its corresponding carbon monolith (HCM-DAH-1) are crack-free in shape. A carbonization process leads to linear and volume shrinkages of ~30% and ~65%,

respectively (taken from the average value of five monoliths). The size of the monolith mainly depends on the container used during the gelation step and, thus, is easy to be enlarged. The synthesis was attempted to scale up by a factor of 5. The obtained carbon product still maintains a perfect monolith shape and exhibits an identical mesostructure (see Figure S1 in the Supporting Information).

Furthermore, the ground HCM-DAH-1 was characterized by TEM and HR-SEM. The TEM images (Figure 2a–c) prove the perfectly regular mesopores of HCM-DAH-1. The images viewed along the [100], [110], and [111] directions, together with the FFT diffractograms, also clearly confirm the presence of an interconnected cubic ($Im3m$) mesopore system.[52,53] The cell parameter estimated from the TEM images is approximately 10.8 nm, which is in good agreement with the value determined from the XRD pattern. HR-SEM images (Figure 2d–e) further verify that HCM-DAH-1 exhibits a long-range and large domain interconnected 3D cubic arrangement. The unit cell parameter and pore size of HCM-DAH-1 estimated from the images are 11.0 and 5.2 nm respectively, which are consistent with the results from XRD, N_2 adsorption, and TEM.

As a monolith material, the mechanical strength of HCM-DAH-1 was measured with a 2 kN intelligent strength tester. Surprisingly, HCM-DAH-1 can bear a load of 15.6 MPa, which is 80 times greater than that reported for a nanocast carbon monolith (27.9 psi, 0.19 MPa)[54] and the recently soft-templated carbon monolith (0.2 MPa).[51] Evidently, our newly developed carbon monolith possesses several salient features such as hierarchical and fully interconnected macropores and mesopores and high mechanical strength, and can be facilely prepared in a time-saving manner.

3.2. Monolithic Carbons Prepared Using Other Organic Amines. To examine the generality of this synthesis, different organic amines, including EDA, DMA, TMA, and TEA, were investigated for the preparation of monolithic carbons (see Table 1). The synthesis conditions follow those used for HCM-DAH-1; however, the amount of the organic amine was adjusted to
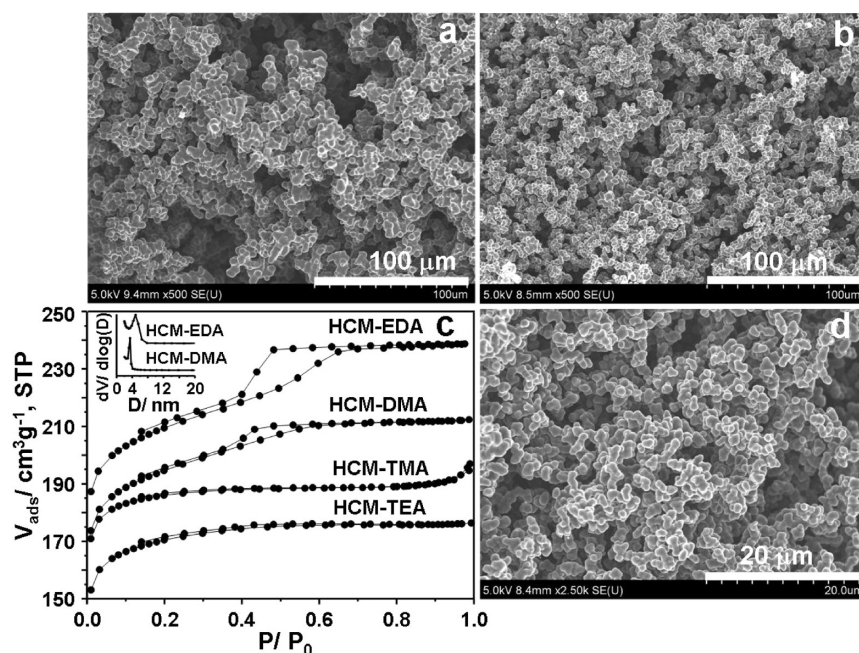
Figure 3. SEM images of HCM-EDA (a), HCM-DMA (b), and HCM-TEA (d); N$_2$ isotherms of HCM-EDA, HCM-DMA, HCM-TMA, and HCM-TEA (c) and the PSDs of HCM-EDA and HCM-DMA (inset). The isotherms of HCM-EDA and HCM-DMA were vertically offset by 20 and 15 cm^3 g^{-1}, STP.

achieve a pH value of the reaction solution identical to that of HCM-DAH-1. The solution of HCM-DAH-1 turned to an opaque white homogeneous emulsion within 1 min, while, for the EDA involved system, an opaque yellow homogeneous emulsion was obtained (see Figure S2). The DMA involved reaction system turned transparent and golden yellow within 5 min, with a gelation period of ~30 min. The TMA and TEA involved systems were quite similar: they gradually turned to pale yellow after 5 min and then to brown and finally solidified within 60 min. After the gelation and aging processes, all these polymers were carbonized under the same conditions as in the case of HCM-DAH-1, and the produced carbon monoliths were correspondingly named as HCM-EDA, HCM-DMA, HCM-TMA, and HCM-TEA (see Table 1).

The SEM images in Figure 3 reveal HCM-EDA and HCM-DMA to be similar to HCM-DAH-1 in their interconnected framework and visible macroporosity. The thickness of the struts is around 0.45 μm. The nitrogen sorption isotherms of HCM-EDA and HCM-DMA are of type IV with a pronounced hysteresis loop in the relative pressure range of 0.4−0.7. This indicates the well-developed mesoporosity. The mesopore sizes are concentrated at ~3.5 nm. The TEM image and XRD pattern (see Figure S3) reveal the ordered mesostructures of these samples. Based on the above analyses, one can conclude that EDA and DMA are also applicable amines for the synthesis of poly(benzoxazine-co-resol)s and their carbonaceous products with hierarchical porosity. However, the monoliths HCM-EDA and HCM-DMA can only withstand pressures of 0.3 and 0.2 MPa, respectively, indicating poor mechanical strength. Obviously, from a mechanical stability point of view, DAH involved HCM-DAH-1 is by far superior to EDA and DMA involved carbon materials.

If TMA or TEA was introduced into the polymerization process, no mesostructures were formed in the resultant carbon HCM-TMA or HCM-TEA. The nitrogen sorption isotherms in

Figure 3c show a microporous feature for these carbons. The amounts of TMA and TEA have been varied with the aim of obtaining mesoporous carbons, however, without success. Evidently, the nature of the organic amines appears to be a crucial factor in determining the assembly of the mesostructure. Upon comparison of the molecular structures of the organic amines listed in Figure S4 (Supporting Information), protic organic bases such as DMA (secondary amine), EDA (primary amine), and DAH (primary amine) seem to favor the formation of ordered mesopores in carbon monoliths. In contrast, aprotic organic bases (TMA and TEA) result in the formation of microporous carbons. Although a series of experiments have been conducted in which the amounts of such aprotic organic bases were varied, no mesoporous carbons could be synthesized. Clearly, aprotic organic bases fail to induce the self-assembly of mesostructures, possibly due to the lack of interaction between TMA (or TEA) and F127 molecules.

In addition, the gel derived from the protic amines (DAH, EDA, and DMA), resorcinol, and formaldehyde was homogeneous in appearance and no sedimentation or macroscopic phase separation was observed during the entire polymerization. The products show remarkably abundant macroporosity, which arises from the cross-linking benzoxazine-containing precursors rather than using additional porogens.[55] This synthesis based on benzoxazine chemistry opens a new pathway for generating hierarchical porosity and intrinsic nitrogen-containing polymer/carbon frameworks, which is of great importance for adsorption and separation.

3.3. Influence of the Amount of DAH Used. On the basis of the aforementioned results, the use of DAH is obviously an ideal option in terms of the synthesis of a porous carbon monolith with an interconnected hierarchical pore system and high mechanical strength. In order to investigate the influence of the DAH concentration on the pore structure, the amount of DAH was varied over the range from 275:2.6 to 275:171.4 (described in
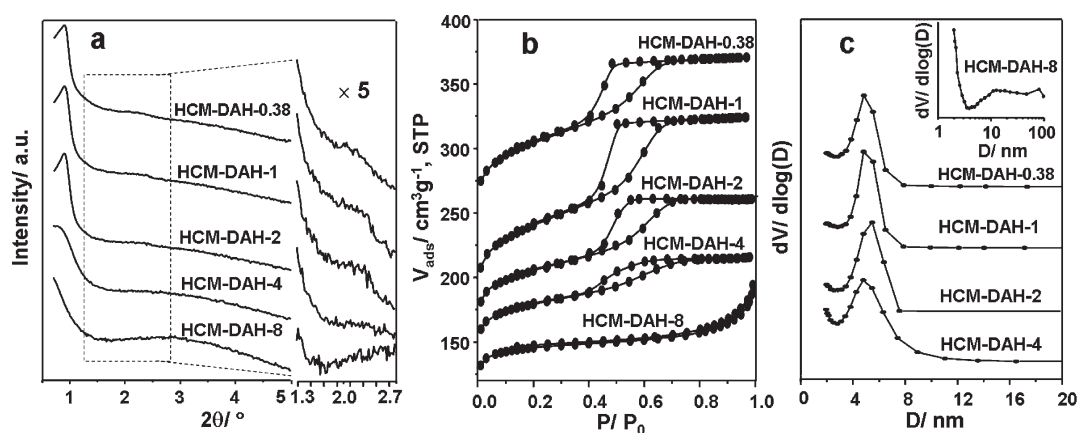
Figure 4. Characterizations of the series HCM-DAH-n with variable DAH concentrations. Low angle XRD patterns (a), N_2 isotherms (b), and the corresponding PSDs (c). The isotherms of HCM-DAH-0.38, HCM-DAH-1, HCM-DAH-2, and HCM-DAH-4 are vertically offset by 130, 50, 20, and 20 cm^3 g^{-1}, STP.
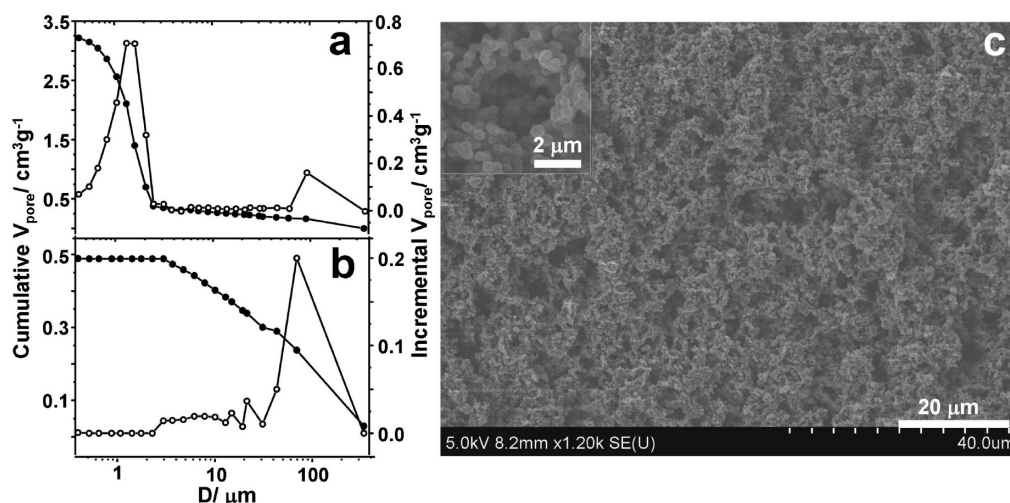
Figure 5. Mercury intrusion curves and differential pore diameter distributions of HCM-DAH-0.38 (a) and HCM-DAH-8 (b); SEM image of HCM-DAH-8 (c).

terms of the molar ratio of R/DAH, see Table 1). As shown in Table 1, samples HCM-DAH-0.38, HCM-DAH-1, HCM-DAH-2, HCM-DAH-4, and HCM-DAH-8 were prepared with a sequentially increased amount of DAH. Their low angle XRD patterns (Figure 4a) reveal that the mesostructural ordering of the carbon monolith is retained with the increasing amount of DAH used up to a level of R/DAH = 275:13.6. However, a further increase leads to loss of the mesostructure (HCM-DAH-8 and HCM-DAH-16), probably due to a fast and uncontrollable reaction rate.

In Figure 4b, the N_2 isotherms of HCM-DAH-0.38 and HCM-DAH-2 are similar to that of HCM-DAH-1, indicating a characteristic of a 3D caged mesopore structure. The PSDs (Figure 4c) show that the majority of the mesopores are concentrated around 5.0 nm. When higher amounts of DAH are used (molar ratio of R/DAH = 275:54.4, sample HCM-DAH-8), it results in less defined mesopores with a relatively broad pore size distribution and a mesopore size concentrated around 12.0 nm. The specific surface area and pore volume show small reductions with the increasing amount of DAH.

The mercury intrusion data show that sample HCM-DAH-0.38, with the lowest amount of DAH used, has a low macropore

volume of ∼0.50 cm^3 g^{-1} (Figure 5a), whereas a pronounced macroporosity with a macropore volume of 3.27 cm^3 g^{-1} was obtained in sample HCM-DAH-8 with the highest amount of DAH (Figure 5b). The SEM image of HCM-DAH-8 (Figure 5c) also reveals a well developed macroporous framework. However, HCM-DAH-8 is easily broken when applying a pressure approaching 0.8 MPa. Evidently, the amount of DAH is crucial in the determination of the meso- and macrostructure assembly, and thus the mechanical stability of the resultant carbon monoliths.

3.4. Insight in the Role of DAH. In order to understand the role of DAH in such unique carbon monoliths, selected as-made polymer materials (HPM-DAH-n series, which correspond to the HCM-DAH-n series, as listed in Table 1) were characterized by $^1H \rightarrow {}^{13}C$ CP/MAS NMR analysis (Figure 6). For comparison, the polymerization of resorcinol with formaldehyde was also catalyzed with NaOH in the absence of organic amines. The obtained resorcinol-formaldehyde polymer was denoted as RF-NaOH. As seen in Figure 6, the spectrum of HPM-DAH-1 shows resolved peaks at ∼53 and 28 ppm, which we assign to the signals of the methylene groups in Ar−CH$_2$−N− and −(CH$_2$)$_6$− respectively, as products from a Mannich reaction. To verify this,

11383

dx.doi.org/10.1021/ja203857g |*J. Am. Chem. Soc.* 2011, 133, 11378–11388
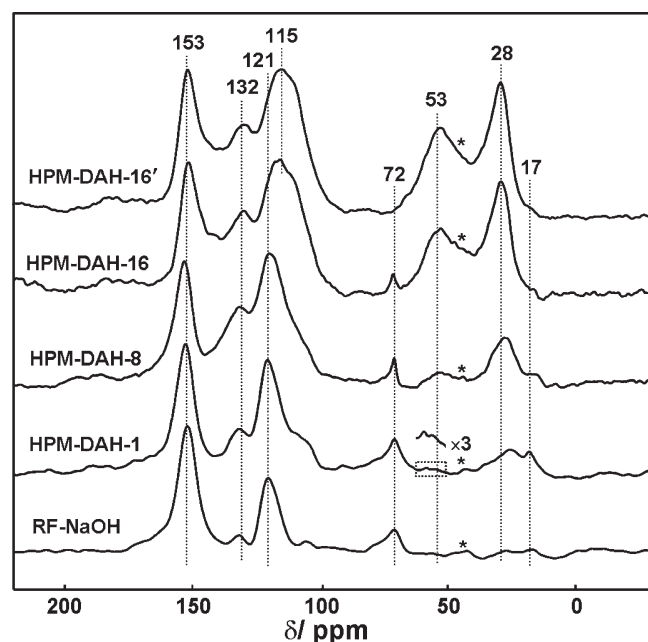
Figure 6. $^1H \rightarrow {}^{13}C$ CP/MAS NMR spectra of the as-made polymer monoliths with different DAH amounts (HPM-DAH-1, HPM-DAH-8, and HPM-DAH-16), the typical phenolic resin monolith (RF-NaOH), and the typical Mannich reaction product, HPM-DAH-16′. Asterisk denotes the spinning sidebands.

the typical polymer RF-NaOH and a typical Mannich reaction product without F127 (denoted HPM-DAH-16′) were used as control samples. In addition, HPM-DAH-8 and HPM-DAH-16 prepared with an increased amount of DAH were also characterized by NMR. It can be clearly seen that, with an increase in the amount of DAH (from HPM-DAH-1 to HPM-DAH-8 and HPM-DAH-16), the intensities of the peaks at ~53 and 28 ppm gradually also increase. This confirms that the Mannich reaction indeed takes place in the polymerization process. In a DAH molecule, the carbon signal of the methylene groups directly connected to $-NH_2$ groups should appear at *ca.* 42 ppm.[56] When the DAH molecule participates in the Mannich reaction, the aforementioned methylene groups should be shifted to 53 ppm.[57,58] As seen in Figure 6, the peak at 53 ppm further confirms that DAH participates in the polymerization by forming polybenzoxazine.

The strong and broad signals with chemical shifts ranging from 100 to 175 ppm are attributed to the carbons in the aromatic rings of resorcinol-formaldehyde or resorcinol-formaldehyde-DAH polymer networks. The broad overlapping signals at *ca.* 28 ppm could also be attributed to the methylene linkages between aromatic rings. The signals at ~72 and 17 ppm correspond to the carbons in the methylene and methyl groups of the block copolymer F127 template.[52,59] These results demonstrate that the as-made poly(benzoxazine-co-resol) polymer monoliths show hybrid characteristics consisting of poly(RF), polybenzoxazine (RF-DAH) segments, and a block copolymer.

Our experiments have demonstrated that the use of the amine DAH results in a quick gelation by the cross-linking reaction of resorcinol, formaldehyde, and DAH within 15 min at 90 °C. This is much quicker than the conventional copolymerization of resorcinol and formaldehyde that requires hours or days[60,61]

(also see Figure S5). As revealed by the NMR analysis, resorcinol, formaldehyde, and DAH can form polybenzoxazine via the Mannich reaction.[62,63] Elemental analyses show that, at the initial reaction stage, the prepolymer contains 3.38 wt % of nitrogen, a similar content of a typical polybenzoxazine.[47] The polybenzoxazine segments subsequently form hydrogen bonds $(Ar-O-H\cdots O)$ with the EO segments of F127 to a significant extent, which can guide the mesostructure assembly between the polymer species and the amphiphilic copolymer template. During the following curing step, the unreacted resorcinol and formaldehyde would copolymerize, or with polybenzoxazine under basic conditions via a condensation reaction. Reaching this stage, the nitrogen content decreases to 0.28 wt %, which is close to the theoretical nitrogen content of 0.32% in the final poly(benzoxazine-co-resol)s. This indicates that polybenzoxazine segments are formed very soon, being the dominant phase in the initial polymerization, while, for the final polymer product, both the polybenzoxazine and the Poly(RF) together form the hybrid skeletons. Such proposed sequential reactions and the stable mesostructure formation mechanism are further proven by the designed experiments and characterizations (see the Supporting Information, Figures S6 and S7).

3.5. CO$_2$ Capture and Separation by the Carbon Monoliths. The capture and separation of CO_2 from the fuel exhaust of power plants has received much attention during the past decade because of the global warming issue.[64] Due to the unique features such as highly interconnected porosity, abundant microporosity, and remarkable mechanical strength, our nitrogen-containing carbon monolith HCM-DAH-1 was evaluated in terms of equilibrium and dynamic CO_2 selectivity and capacities as well as other important parameters such as adsorption thermodynamics, regenerability, and stability. To increase the surface area and further modify the pore system of the carbon monolith, HCM-DAH-1 was also activated by CO_2 at 900 °C for either 1 or 3 h. The obtained samples are denoted HCM-DAH-1-900-1 (S_{BET}: 1392 m^2 g^{-1}) and HCM-DAH-1-900-3 (S_{BET}: 2160 m^2 g^{-1}). Their N_2 sorption isotherms are shown in Figure S8.

The equilibrium CO_2 (at 0 and 25 °C) and N_2 (at 25 °C) isotherms of sample HCM-DAH-1, HCM-DAH-1-900-1, and HCM-DAH-1-900-3 are accordingly shown in Figure 7a−c. There are three distinct regimes in the CO_2 isotherms. As described for CO_2 adsorption in MOFs,[65] at low pressures, uptake in different monoliths correlates with the heat of adsorption; at intermediate pressures, uptakes correlate with the monolith surface area; and at the highest pressures, uptakes correlate with the free volume available within the monoliths. At 0 °C, HCM-DAH-1 shows a high CO_2 adsorption capacity of 3.3 mmol g^{-1} at 780 mmHg, which corresponds with three CO_2 molecules per nm^2. The maximum CO_2 uptake of HCM-DAH-1-900-1 and HCM-DAH-1-900-3 are 4.9 and 4.5 mmol g^{-1}, respectively, which is superior to the reported carbons[10] and close to the bio-MOF-11[32] (by far the highest equilibrium CO_2 capacity measured under atmospheric pressure). In particular, the CO_2 uptake (1.6 mmol g^{-1}) of HCM-DAH-1 at a low pressure of 115 mmHg (which is a typical partial pressure of CO_2 in flue gases) outperforms that of the widely used activated carbons (e.g., Norit R1 Extra, BPL, Maxsorb, A10 fiber).[10] At 25 °C and 780 mmHg, the maximum CO_2 uptakes of HCM-DAH-1, HCM-DAH-1-900-1, and HCM-DAH-1-900-3 are 2.6, 3.3, and 2.9 mmol g^{-1}, respectively. These values, under the same sorption conditions, rival the highest capacities of the widely used activated carbons (<2 mmol g^{-1}),[10] the soft-templated mesoporous carbons

11384

dx.doi.org/10.1021/ja203857g |*J. Am. Chem. Soc.* 2011, 133, 11378–11388
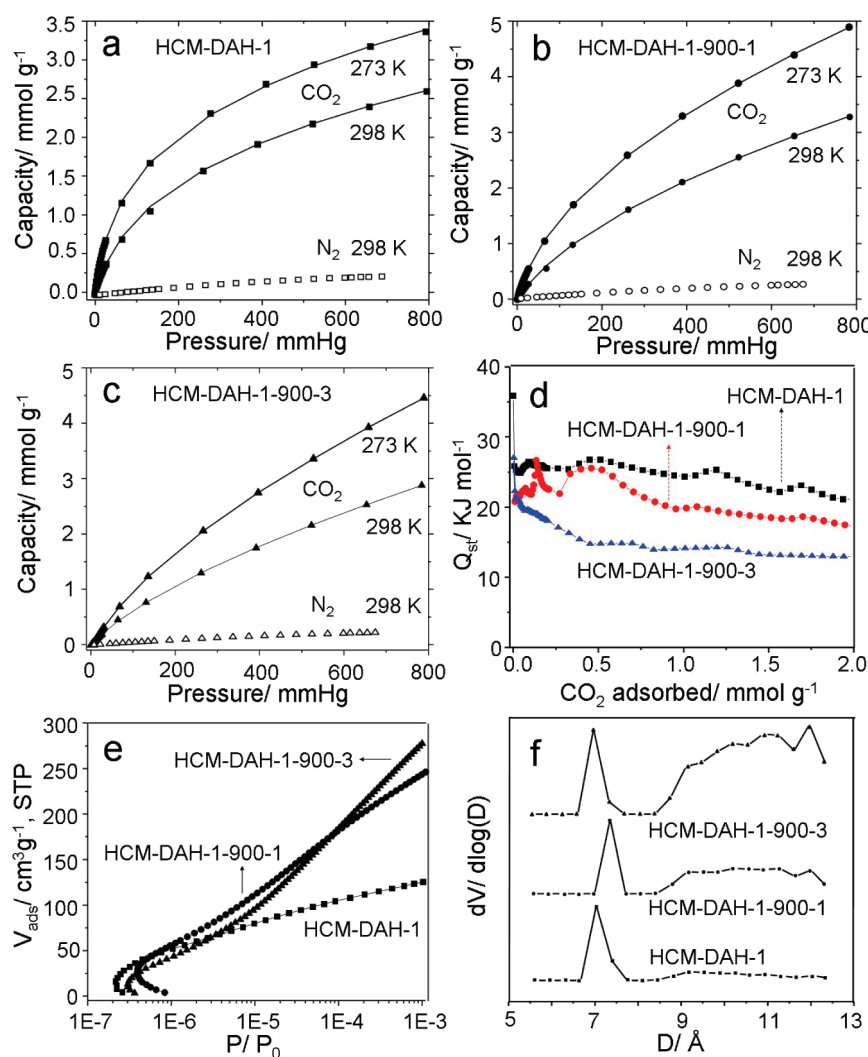
Figure 7. CO_2 and N_2 adsorption isotherms under equilibrium conditions: Adsorption isotherms (a, b, c) for CO_2 (filled symbols) at 0 and 25 °C and for N_2 (open symbols) at 25 °C, where the solid line represents a Toth model fit to the CO_2 isotherm; (d) Isosteric heat of adsorption for CO_2 at different CO_2 loadings; (e, f) N_2 adsorption isotherms at −196 °C and low pressures ($1.0 \times 10^{-7} < P/P_0 < 1.0 \times 10^{-3}$) and the corresponding PSDs calculated using the DFT method.

(2.39 mmol g^{-1}),[66] and the hard-templated CMK-3 (1.7 mmol g^{-1}).[67] The uptakes of these monoliths are comparable or even superior to those of powder ZIF-81, ZIF-82, ZIF-95, and bio-MOF-11.[27,28,32] This indicates that our mechanically stable carbon monoliths can be good sorbents due to a high CO_2 capacity and no additional shaping process was required, which is in contrast to powder MOFs or zeolites

Comparatively, the maximum N_2 uptake of samples HCM-DAH-1, HCM-DAH-1-900-1 and HCM-DAH-1-900-3 at 25 °C is only 0.27, 0.29, and 0.26 mmol g^{-1}, respectively. The initial slopes of the CO_2 and N_2 adsorption isotherms were calculated, and the ratios of these slopes were used to estimate the adsorption selectivity for CO_2 over N_2 (see Figure S9 for details of selectivity calculations). As a result, the CO_2/N_2 selectivities of HCM-DAH-1, HCM-DAH-1-900-1, and HCM-DAH-1-900-3 are 28:1, 17:1, and 13:1 at 25 °C, respectively. To our knowledge, the selectivity of HCM-DAH-1 toward CO_2 is by far the highest among the known micro-/mesoporous carbon materials.[28,35,68]

The steepness of the rise in the isotherm, especially at low pressures, indicates a relatively strong CO_2 binding interaction,

particularly for HCM-DAH-1. The CO_2 adsorption isotherms of these three carbons differ significantly in their slopes. Indeed, by fitting the CO_2 adsorption isotherms measured at 0 and 25 °C and applying a variant of the Clausius−Clapeyron equation, the isosteric heats of adsorption (Q_{st}) were calculated to lie in the range 21.1−35.9, 19.6−26.7, and 13.2−26.9 kJ mol^{-1} for HCM-DAH-1, HCM-DAH-1-900-1, and HCM-DAH-1-900-3, respectively (see Figure 7d and the calculation details in the Supporting Information). The higher Q_{st} in the initial stage leads to a preferential adsorption of CO_2 over N_2, which can be interpretated as the strong quadrupolar interactions of CO_2 molecules with the heterogeneous micropore walls (e.g., nitrogen groups) at low pressures.[26,28]

Figure 7e−f show the N_2 adsorption isotherms of HCM-DAH-1, HCM-DAH-1-900-1, and HCM-DAH-1-900-3 under a low relative pressure range of 1.0×10^{-7}−1.0×10^{-3} and the corresponding micropore size distributions. Clearly, activation causes a remarkable uptake of isotherms (Figure 7e). As seen in Figure 7f, these three samples all contain micropores with the sizes ranging from 7.0 to 7.4 Å. The widths of the micropores are
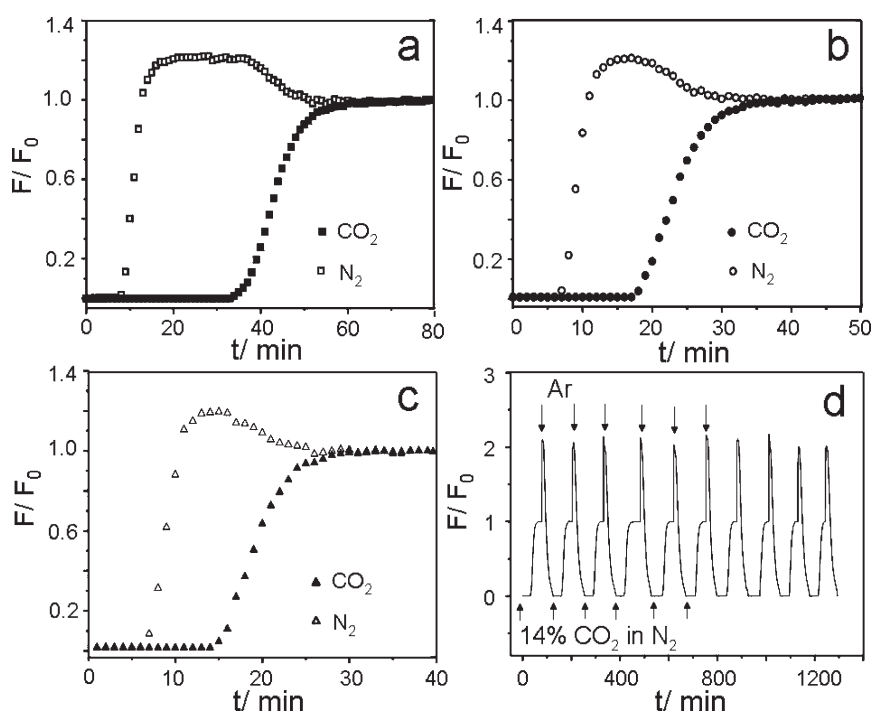
Figure 8. (a, b, c) Breakthrough curves, a 14% mixture of CO_2 in N_2 is fed into a bed of HCM-DAH-1, HCM-DAH-1-900-1, and HCM-DAH-1-900-3, respectively. (d) Recycle runs of CO_2 adsorption−desorption on HCM-DAH-1 at 25 °C, using a stream of 14% (v/v) CO_2 in N_2, followed regeneration by Ar flow.

twice as large as the kinetic diameter of CO_2 (∼3.3 Å). These small micropores are responsible for the strong adsorption of CO_2 molecules.[69] Although an additional activation results in HCM-DAH-1-900-1 and HCM-DAH-1-900-3 having much larger surface areas and newly generated micropores with a length scale of 9−13 Å, they do not show higher CO_2 uptake at the low relative pressure than that of HCM-DAH-1, simply because the relatively larger micropores (9−13 Å) are effective as a rapid transport path rather than as trapping sites for CO_2.[28] This reveals that abundant small micropores (∼7.0 Å) showing high adsorption potential are essential for a CO_2 capture material to show high performances.

In addition to the equilibrium uptake measurements, we conducted the dynamic "breakthrough" separation experiments on our carbon monoliths to determine its CO_2 separation capacity, using a flow of 14% (v/v) CO_2 balanced with N_2 (see Figure S10 for details), which approximately mimics a flue gas. The resulting "breakthrough curve" (Figure 8a−c) demonstrates that the three samples can completely separate CO_2 from the N_2 stream. From the breakthrough curves, a calculated mass uptake capacity of HCM-DAH-1, HCM-DAH-1-900-1, and HCM-DAH-1-900-3 is accordingly 4.1 wt %, 3.3 wt %, and 2.7 wt % CO_2, which are coincident with the single component CO_2 adsorption datum at the partial pressure of 115 mmHg. In addition, the separation factors α for CO_2 over N_2 is estimated to be 27.8, 14.6, and 13.2 for HCM-DAH-1, HCM-DAH-1-900-1, and HCM-DAH-1-900-3, respectively (the calculation details in the Supporting Information). The selectivity of HCM-DAH-1 is higher than that of widely used BPL carbon (α: 11.1),[27] ZIF-79 (α: ∼22),[27] ZIF-95 (α: 18.0 ± 1.7),[28] and PCPs (α: 22−27)[35] and is comparable to that of ZIF-81 (α: ∼25)[27] and ZIF-100 (α: 25.0 ± 2.4).[28] These dynamic data provide clear evidence that HCM-DAH-1 is extremely selective for adsorbing CO_2 over

N_2 and represents a major advance in the CO_2 separation capacity for carbon materials.

The gas cycling experiments also verified the selective and reversible CO_2 capture capacity of HCM-DAH-1. A sample saturated with CO_2 was subjected to an argon purge flow at 15 mL/min at 25 °C. After approximately 60 min, no CO_2 was detected in the effluent (Figure 8d). Successive regeneration experiments reveal that HCM-DAH-1 retains 95−99% of its intrinsic capacity after such mild regeneration conditions. Further cycling does not lead to a visible reduction of the capacity. Although regeneration methods in an industrial process would likely involve some combination of flow, pressure, and temperature modulation, these tests signify that HCM-DAH-1 provides a high-capacity separation with very mild conditions for regeneration, which makes it outperform many other porous solids.[8,24,25,70] For example, zeolites,[71] amine-modified silicas,[24,25] and MOFs[68] would require thermal activation or vacuum for the regeneration. Materials with the properties such as high CO_2 capture capacity and low energy consumption for CO_2 release are more desirable for practical applications.

Commonly, the separation efficacy of a physisorbent (e.g., zeolites, MOFs, etc.) decreases under a humid medium. To examine the moisture tolerance of our carbon monolith, we further tested its CO_2 sorption and separation ability using a gas mixture of $CO_2/N_2/H_2O$ (v/v/v, 14/83.5/2.5). The breakthrough results as representatively shown in Figure S11 reveal that HCM-DAH-1 provides a surprisingly complete separation of CO_2 from the N_2 and H_2O stream. The calculated dynamic capacity is 4%, which is almost identical to that measured under drying conditions. The measurements were repeated 3 times, and all gave nearly identical results. The measured water contact angle is ∼128° (for more detail see Figure S12), indicating the hydrophobic surface of HCM-DAH-1. These preliminarily

results reveal that our carbon monolith also shows a high performance for CO_2 separation under humid conditions.

4. CONCLUSIONS

We have developed a new synthesis of porous carbon monoliths derived from poly(benzoxazine-co-resol) polymers, which have fully interconnected macropores and mesopores, a nitrogen-containing carbon framework, high mechanical strength, and high selectivity and uptake for CO_2 capture. In this synthesis, the use of amines leads to not only nitrogen incorporation in the framework but also a short synthesis period (gelation within 10−15 min at 90 °C). The synthesis can be scaled up easily to prepare larger amounts of polymer (carbon) monoliths with identical mesostructures. The CO_2 capture and separation results show that the poly(benzoxazine-co-resol)-based carbon sorbents perform well in CO_2 uptakes, selectivity, and regeneration among the commercial and state-of-the-art carbon sorbents reported to date. We believe that this study provides a new approach for the development of novel nitrogen-doped carbon sorbents by the benzoxazine chemistry which offers a high degree of flexibility in the molecular design of monomers (phenols, aldehydes, and diamines). This synthesis may have a major impact on the advance of new types of materials for CO_2 capture and separation from flue gases.

■ ASSOCIATED CONTENT

⑤ Supporting Information. The sample characterizations including N_2 isotherm, optical images, TEM image, low-angle XRD, molecular structures of the amines, TG and DTG curves as well as the designed experiments to demonstrate the sequential reactions in the formation of the monoliths. Full details of breakthrough curve measurements and calculations of selectivity and capacity for CO_2 capture. This material is available free of charge via the Internet at http://pubs.acs.org.

■ AUTHOR INFORMATION

Corresponding Author
anhuilu@dlut.edu.cn

■ ACKNOWLEDGMENT

■ REFERENCES

(1) Song, C. *Catal. Today* **2006**, *115*, 2.
(2) Yu, K. M. K.; Curcic, I.; Gabriel, J.; Tsang, S. C. *ChemSusChem* **2008**, *1*, 893.
(3) Sakakura, T.; Choi, J. C.; Yasuda, H. *Chem. Rev.* **2007**, *107*, 2365.
(4) White, C. M.; Strazisar, B. R.; Granite, E. J.; Hoffman, J. S.; Pennline, H. W. *J. Air Waste Manage. Assoc.* **2003**, *53*, 645.

(5) Demessence, A.; D'Alessandro, D. M.; Foo, M. L.; Long, J. R. *J. Am. Chem. Soc.* **2009**, *131*, 8784.
(6) Morris, R. E.; Wheatley, P. S. *Angew. Chem., Int. Ed.* **2008**, *47*, 4966.
(7) D'Alessandro, D. M.; Smit, B.; Long, J. R. *Angew. Chem., Int. Ed.* **2010**, *49*, 6058.
(8) Choi, S.; Drese, J. H.; Jones, C. W. *ChemSusChem* **2009**, *2*, 796.
(9) Thote, J. A.; Iyer, K. S.; Chatti, R.; Labhsetwar, N. K.; Biniwale, R. B.; Rayalu, S. S. *Carbon* **2010**, *48*, 396.
(10) Himeno, S.; Komatsu, T.; Fujita, S. *J. Chem. Eng. Data* **2005**, *50*, 369.
(11) Wahby, A.; Ramos-Feránndez, J. M.; Martínez-Escandell, M.; Sepúlveda- Escribano, A.; Silvestre-Albero, J.; Rodríguez-Reinoso, F. *ChemSusChem* **2010**, *3*, 974.
(12) Dillon, E. P.; Crouse, C. A.; Barron, A. R. *ACS Nano* **2008**, *2*, 156.
(13) Wu, Z.; Hao, N.; Xiao, G.; Liu, L.; Webley, P.; Zhao, D. *Phys. Chem. Chem. Phys.* **2011**, *13*, 2495.
(14) Bezerra, D. P.; Oliveira, R. S.; Vieira, R. S.; Cavalcante, C. L., Jr; Azevedo, D. C. S. *Adsorption* **2011**, *17*, 235.
(15) Zhao, L.; Bacsik, Z.; Hedin, N.; Wei, W.; Sun, Y.; Antonietti, M.; Titirici, M.-M. *ChemSusChem* **2010**, *3*, 840.
(16) Pevida, C.; Drage, T. C.; Snape, C. E. *Carbon* **2008**, *46*, 1464.
(17) Cavenati, S.; Grande, C. A.; Rodrigues, A. E. *J. Chem. Eng. Data* **2004**, *49*, 1095.
(18) Wang, Y.; LeVan, M. D. *J. Chem. Eng. Data* **2009**, *54*, 2839.
(19) Lee, Y.; Liu, D.; Seoung, D.; Liu, Z.; Kao, C.-C.; Vogt, T. *J. Am. Chem. Soc.* **2011**, *133*, 1674.
(20) Sayari, A.; Belmabkhout, Y. *J. Am. Chem. Soc.* **2010**, *132*, 6312.
(21) Serna-Guerrero, R.; Da'na, E.; Sayari, A. *Ind. Eng. Chem. Res.* **2008**, *47*, 4761.
(22) Yue, M. B.; Chun, Y.; Cao, Y.; Dong, X.; Zhu, J. H. *Adv. Funct. Mater.* **2006**, *16*, 1717.
(23) Hicks, J. C.; Drese, J. H.; Fauth, D. J.; Gray, M. L.; Qi, G.; Jones, C. W. *J. Am. Chem. Soc.* **2008**, *130*, 2902.
(24) Ma, X. L.; Wang, X. X.; Song, C. S. *J. Am. Chem. Soc.* **2009**, *131*, 5777.
(25) Chen, C.; Yang, S.-T.; Ahn, W.-S.; Ryoo, R. *Chem. Commun.* **2009**, 3627.
(26) Vaidhyanathan, R.; Iremonger, S. S.; Shimizu, G. K. H.; Boyd, P. G.; Alavi, S.; Woo, T. K. *Science* **2010**, *330*, 650.
(27) Banerjee, R; Furukawa, H.; Britt, D.; Knobler, C.; O'Keeffe, M.; Yaghi, O. M. *J. Am. Chem. Soc.* **2009**, *131*, 3875.
(28) Wang, B.; Côté, A. P.; Furukawa, H.; O'Keeffe, M.; Yaghi, O. M. *Nature* **2008**, *453*, 207.
(29) Britt, D.; Furukawa, H.; Wang, B.; Glover, T. G.; Yaghi, O. M. *Proc. Natl. Acad. Sci. U.S.A.* **2009**, *106*, 20637.
(30) Yazaydın, A.Ö.; Snurr, R. Q.; Park, T.-H.; Koh, K.; Liu, J.; LeVan, M. D.; Benin, A. I.; Jakubczak, P.; Lanuza, M.; Galloway, D. B.; Low, J. J.; Willis, R. R. *J. Am. Chem. Soc.* **2009**, *131*, 18198.
(31) Zheng, S.; Wu, T.; Zhang, J.; Chow, M.; Nieto, R. A.; Feng, P.; Bu, X. *Angew. Chem., Int. Ed.* **2010**, *49*, 5362.
(32) An, J.; Geib, S. J.; Rosi, N. L. *J. Am. Chem. Soc.* **2010**, *132*, 38.
(33) Choi, H.-S.; Suh, M. P. *Angew. Chem., Int. Ed.* **2009**, *48*, 6865.
(34) Llewellyn, P. L.; Bourrelly, S.; Serre, C.; Filinchuk, Y.; Férey, G. *Angew. Chem., Int. Ed.* **2006**, *45*, 7751.
(35) Nakagawa, K.; Tanaka, D.; Horike, S.; Shimomura, S.; Higuchi, M.; Kitagawa, S. *Chem. Commun.* **2010**, *46*, 4258.
(36) Liang, C. D.; Li, Z. J.; Dai, S. *Angew. Chem., Int. Ed.* **2008**, *47*, 3696.
(37) Lu, A.-H.; Schüth, F. *Adv. Mater.* **2006**, *18*, 1793.
(38) Lee, J.; Kim, J.; Hyeon, T. *Adv. Mater.* **2006**, *18*, 2073.
(39) Lohe, M. R.; Rose, M.; Kaskel, S. *Chem. Commun.* **2009**, 6056.
(40) Kadib, A. E.; Chimenton, R.; Sachse, A.; Fajula, F.; Galarneau, A.; Coq, B. *Angew. Chem., Int. Ed.* **2009**, *48*, 4969.
(41) Williams, J. L. *Catal. Today* **2001**, *69*, 3.
(42) Davis, M. E. *Nature* **2002**, *417*, 813.
(43) Lee, K. B.; Beaver, M. G.; Caram, H. S.; Sircar, S. *Ind. Eng. Chem. Res.* **2008**, *47*, 8048.
(44) Li, J.-R.; Kuppler, R. J.; Zhou, H.-C. *Chem. Soc. Rev.* **2009**, *38*, 1477.

(45) Yagci, Y.; Kiskan, B.; Ghosh, N. N. *J. Polym. Sci., Part A: Polym.* **2009**, *47*, 5565.

(46) Allen, D. J.; Ishida, H. *Polymer* **2007**, *48*, 6763.

(47) Goward, G. R.; Sebastiani, D.; Schnell, I.; Spiess, H. W.; Kim, H.-D.; Ishida, H. *J. Am. Chem. Soc.* **2003**, *125*, 5792.

(48) Matos, J. R.; Kruk, M.; Mercuri, L. P.; Jaroniec, M.; Zhao, L.; Kamiyama, T.; Terasaki, O.; Pinnavaia, T. J.; Liu, Y. *J. Am. Chem. Soc.* **2003**, *125*, 821.

(49) Liang, C.; Dai, S. *Chem. Mater.* **2009**, *21*, 2115.

(50) Nakanishi, K; Tanaka, N. *Acc. Chem. Res.* **2007**, *40*, 863.

(51) Huang, Y.; Cai, H.; Feng, D.; Gu, D.; Deng, Y.; Tu, B.; Wang, H.; Webley, P. A.; Zhao, D. *Chem. Commun.* **2008**, 2641.

(52) Meng, Y.; Gu, D.; Zhang, F.; Shi, Y.; Cheng, L.; Feng, D.; Wu, Z.; Chen, Z.; Wan, Y.; Stein, A.; Zhao, D. *Chem. Mater.* **2006**, *18*, 4447.

(53) Sakamoto, Y.; Kaneda, M.; Terasaki, O.; Zhao, D.; Kim, J.; Stucky, G.; Shin, H.; Ryoo, R. *Nature* **2000**, *408*, 449.

(54) Wang, X.; Bozhilov, K. N.; Feng, P. *Chem. Mater.* **2006**, *18*, 6373.

(55) Mayes, R. T.; Tsouris, C.; Kiggans, J. O.; Mahurin, S. M.; DePaoli, D. W.; Dai, S. *J. Mater. Chem.* **2010**, *20*, 8674.

(56) Wei, Y.; Tian, Z.; Gies, H; Xu, R.; Ma, H.; Pei, R.; Zhang, W.; Xu, Y.; Wang, L.; Li, K.; Wang, B.; Wen, G.; Lin, L. *Angew. Chem., Int. Ed.* **2010**, *49*, 5367.

(57) Allen, D. J.; Ishida, H. *J. Appl. Polym. Sci.* **2006**, *101*, 2798.

(58) Laobuthee, A.; Chirachanchai, S.; Ishida, H.; Tashiro, K. *J. Am. Chem. Soc.* **2001**, *123*, 9947.

(59) Liu, Y. R. *Microporous Mesoporous Mater.* **2009**, *124*, 190.

(60) Pekala, R. W. *J. Mater. Sci.* **1989**, *24*, 3221.

(61) Al-Muhtaseb, S. A.; Ritter, J. A. *Adv. Mater.* **2003**, *15*, 101.

(62) Kiskan, B.; Yagci, Y. *Macromol. Symp.* **2010**, *298*, 145.

(63) Men, W.; Lu, Z. *J. Appl. Polym. Sci.* **2007**, *106*, 2769.

(64) Granite, E. J.; Pennline, H. W. *Ind. Eng. Chem. Res.* **2002**, *41*, 5470.

(65) Yang, Q.; Zhong, C.; Chen, J. *J. Phys. Chem. C* **2008**, *112*, 1562.

(66) Saha, D.; Deng, S. *J. Colloid Interface Sci.* **2010**, *345*, 402.

(67) Chandrasekar, G.; Son, W.-J.; Ahn, W.-S. *J Porous Mater.* **2009**, *16*, 545.

(68) Hao, G.-P.; Li, W.-C.; Lu, A.-H. *J. Mater. Chem.* **2011**, *21*, 6447.

(69) Vishnyakov, A.; Ravikovitch, P. I.; Neimark, A. V. *Langmuir* **1999**, *15*, 8736.

(70) Liu, J.; Wang, Y.; Benin, A. I.; Jakubczak, P.; Willis, R. R.; LeVan, M. D. *Langmuir* **2010**, *26*, 14301.

(71) Harlick, P. J. E.; Tezel, F. H. *Microporous Mesoporous Mater.* **2004**, *76*, 71.